Electrically controlled on-demand photon transfer between high-Q photonic crystal nanocavities on a silicon chip

Masahiro Nakadai[1,a)], Takashi Asano[1,*] and Susumu Noda[1, 2, *]

[1]Department of Electronic Science and Engineering, Kyoto University, Kyoto 615-8510, Japan
[2]Photonics and Electronics Science and Engineering Center, Kyoto University, Kyoto 615-8510, Japan

[a]) e-mail: nakadai@qoe.kuee.kyoto-u.ac.jp
* Author to whom correspondence should be addressed: tasano@qoe.kuee.kyoto-u.ac.jp and snoda@qoe.kuee.kyoto-u.ac.jp

Abstract

Optical buffer memories, which do not rely on an intermediate conversion between optical and electrical signals, can be used to realize optical networks with low latency and low energy consumption. Photonic crystal nanocavities can confine photons in a very small region for a long time, and thus may be used as core components of such optical buffer memories. However, a scalable method for on-demand photon transfer between nanocavities is required. Here, we demonstrate a photonics–electronics integration solution that realizes electrical control of a coupled ultra-high quality-factor nanocavity system on a silicon chip. In this system, the photons confined in one of the two storage nanocavities can be transferred to the other storage nanocavity by applying a voltage pulse to the control cavity. A transfer efficiency of 76% and a cavity photon lifetime of 1.3 ns after the transfer are achieved.

Introduction

Photonic devices on silicon (Si) chips that are based on nanowire waveguides or photonic crystals (PCs), have been considered as technologies that can expand the range of applications for optical interconnects, optical communication, optical sensing, and optical information processing[1–6]. So far, photonic devices such as modulators, filters, and their dense integration have been realized based on Si nanowire waveguides[3,4]. Moreover, it has also become possible to monolithically integrate III–V-based light sources and photodetectors on these devices[6]. Such integrated systems on Si chips are being utilized as low-cost modules for conversion between electrical and optical signals used in rack-to-rack, board-to-board, and chip-to-chip optical interconnections[4,6]. On the other hand, two-dimensional PCs can provide structures with properties that cannot be achieved with nanowire waveguides, such as waveguiding structures with very low group velocities[2] and cavities with long photon lifetimes and small modal volumes[1,5,7]. In particular, nanocavities based on PCs have the potential to be utilized as optical buffer memories, which do not rely on energy consuming photon–electron–photon conversion processes.

To understand the potential of the PC-based technology for optical buffering, we studied the improvement of the photon lifetimes in PC nanocavities and the manipulation of photons using coupled PC nanocavity systems. We demonstrated a very long photon lifetime of 9.2 ns together with a small modal volume of 1.6 cubic wavelengths in a Si PC nanocavity operating at telecommunication wavelengths[7]. We also reported on the optically controlled photon

transfer between PC nanocavities on a Si chip[8]. In this proof-of-concept of optical buffering using nanocavities, photons confined in a storage nanocavity with a photon lifetime of 0.2 ns were transferred to another storage nanocavity by decreasing the refractive index of a control nanocavity located between the two storage cavities. The refractive index of the control cavity was changed by irradiating a 20-ps light pulse that generated free carriers to induce a blue-shift of the cavity resonance wavelength via the carrier plasma effect[3]. However, this optical control method requires not only an external optical system of a size much larger than the chip itself, but also a complex optical control of different control pulse timings if many cavities need to be controlled, making it practically impossible to scale up the system. The implementation of an electrical refractive-index-control mechanism can in principle improve the scalability, but techniques need to be developed that allow us to introduce such a mechanism, while keeping the photon storage times in the nanocavities sufficiently long.

In this work, we demonstrate a photonics–electronics integration solution that realizes electrical control of a coupled ultra-high quality(Q)-factor nanocavity system on a Si chip. The fabricated system has an integrated refractive-index-control mechanism based on an in-plane *p-i-n*-diode, and an efficient photon transfer between the storage nanocavities is possible by applying an electrical control pulse. The important design elements of the PC structure in this system were optimized using a machine-learning-based method to realize a large coupling coefficient between the nanocavities, while preserving the high Q factors. We also developed fabrication methods that can reduce contamination of the cavities during the fabrication of the *p-i-n* diode. The developed system achieves a transfer efficiency of 76% and a cavity photon lifetime of 1.3 ns (corresponding to a Q factor of 1.6 million) after the transfer. This control scheme will help to realize optical buffer memories that provide on-demand storage and extraction of photonic information on a chip.

Results

Sample design. The fabricated PC chip with an electrical refractive-index-control mechanism is shown in Fig. 1a. We mounted the PC chip on a ceramic package as shown in the figure. For the chip fabrication, we used a silicon-on-insulator (SOI) substrate, and the PC structure was formed in the 220-nm-thick top Si layer of the SOI substrate. Figure 1b shows a microscopic image of the region on the chip that contains the coupled nanocavity system. The main elements of this device are the three nanocavities A, B, and C (the three short horizontal orange lines in the figure), which are coupled via the two coupling waveguides (each is about 40 μm long) slightly above them and have a third long excitation waveguide below them. Figure 1c shows a scanning electron microscopy (SEM) image of the control nanocavity and the three waveguides in its vicinity. Figure 1d clarifies the design of the used photonic heterostructure nanocavities[9]; the holes of the PC have a diameter of 220 nm, and the PC lattice constant in the horizontal direction is larger at the center. The hole patterns in the vicinity of the cavities and coupling waveguides were designed by the assistance of a machine-learning-based optimization method [10]. The arrows indicate those holes that have been shifted from their original position in the PC lattice according to the optimization result (an expanded view of the structure is shown in Supplementary Fig. S1). The SiO_2 layer underneath the PC was removed to enable strong light confinement by symmetric air cladding.

In Fig. 1b, we see that cavity C is located in the *i*-region of an in-plane *p*-*i*-*n* diode. This enables us to conveniently change the resonance wavelength of cavity C, λ_C, via the carrier plasma effect by changing the carrier density in the *i*-region electrically[11]. This design has the advantage that free-carrier absorption can be reduced at zero bias. We used a doping density of 3×10^{19} cm^{-3} for both the *p*- and *n*-regions and the width of the *i*-region was set to 4.5 μm to realize a sufficiently high modulation speed of λ_C, $|d\lambda_C/dt|$, while maintaining a sufficiently small optical absorption loss at zero bias. Nanocavities A and B were used to store photons. To control their resonance wavelengths (λ_A and λ_B, respectively), we used micro-heaters; λ_A and λ_B can be almost independently controlled and tuned within a range of 1560 to 1561 nm by the microheaters via the thermo-optic effect[12]. The coupling between nanocavities A and C was achieved by the left coupling waveguide, whose Fabry-Perot modes do not overlap with the resonance wavelengths of the nanocavities, thereby effectively achieving a direct coupling between them[13]. The same design was used for the coupling between nanocavities C and B.

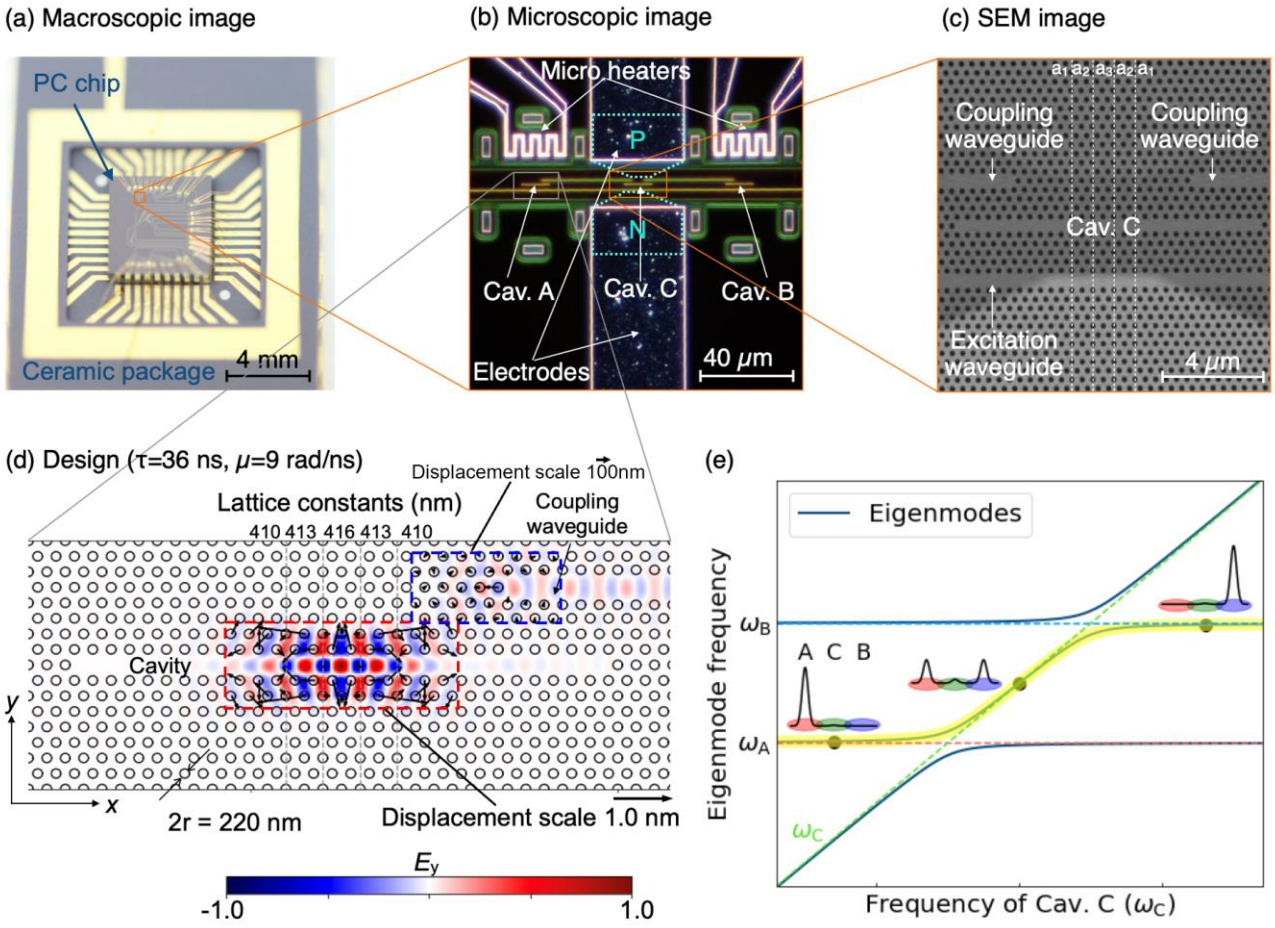

Fig. 1| The fabricated PC chip. a, The chip mounted on a ceramic package. **b,** Microscopic image of the coupled nanocavity system on the chip. **c,** SEM image of the control nanocavity and the waveguides. The heterostructure nanocavity geometry is basically defined by the three different lattice constants of the PC, $a_1 = 410$ nm, $a_2 = 413$ nm, and $a_3 = 416$ nm. **d,** Detailed geometry of nanocavity A and the left coupling waveguide (the other structures also use this design). The result of the fine-tuning of the air-hole positions is shown by the displacement arrows. The length scale of the arrows of the cavity region is indicated below the figure, and that of the waveguide region is indicated above. The radii of the air holes are $r = 110$ nm. The distribution of the *y* component of the electric field of the resonant mode is

plotted with blue and red colors. **e,** Conceptual diagram showing the eigenstates of the system when the angular resonance frequency of nanocavity C is changed.

Optimum operating conditions. The principle of the photon transfer is explained with the diagram in Fig. 1e, where we define the angular resonance frequencies of nanocavities A, B, and C, as ω_A, ω_B, and ω_C, respectively. The transfer is based on an adiabatic process and the frequencies of the eigenstates of the coupled cavity system change as a function of ω_C due to strong coupling, which results in an anti-crossing behavior. In our device, photons are first injected into nanocavity A using the excitation waveguide while $\omega_C \ll \omega_A$. Then, these photons can be transferred adiabatically to nanocavity B along the yellow-highlighted eigenmode in Fig. 1e by increasing ω_C up to a frequency satisfying $\omega_B \ll \omega_C$[8,14]. The details of the operating principle are given in the Supplementary Information. To keep the transfer efficiency close to unity, it is necessary to fulfill the condition $|d\omega_C/dt| \ll 2\pi\mu^2$ according to Landau and Zener[15]. Here, μ is the cavity–cavity coupling constant. However, when free-carrier injection is used to control ω_C, a loss will occur in the region $\omega_A \leq \omega_C \leq \omega_B$, because here the photons partially exist in nanocavity C (see the middle inset of Fig. 1e) and free-carrier absorption takes place. In order to avoid this loss, $|d\omega_C/dt|$ needs to be increased to pass through this region quickly. According to a detailed theoretical study of our system[14], the highest transfer efficiency for a given μ can be achieved by adjusting the value of $\omega_B - \omega_A$ to about 0.8μ and using $|d\omega_C/dt| \simeq 0.2 \times 2\pi\mu^2$. Also from the viewpoint of applications, a faster change in ω_C is preferable because the time required to complete the transfer can be shortened, leading to faster writing and reading speeds associated with optical buffering. Therefore, a method to increase μ needs to be developed. In addition, the photon lifetimes of the actually fabricated nanocavities (especially for A and B) are important, because a longer photon lifetime means a longer storage time of the buffered photonic information.

There are two issues in realizing a large μ and a long photon lifetime τ. Firstly, in order to realize a large μ, it is necessary to introduce the coupling waveguides as close to the nanocavities as possible. However, the closer the coupling waveguide is, the greater is the disturbance of the cavity-mode field. Since this disturbance increases the radiation loss of the nanocavity, there is a fundamental trade-off relationship between μ and τ. Secondly, τ depends not only on the cavity structure but also on the degree of optical absorption caused by impurities inside or on the surface of the material[7,16]. Because we need to introduce a *p-i-n* structure, which increases the complexity in the fabrication process, the degree of contamination of the nanocavity is likely to become larger. Therefore, the introduction of a *p-i-n* structure can reduce τ. In order to solve these problems, we developed a new advanced design method based on machine learning and also developed fabrication methods that can suppress the contamination of the nanocavity during impurity activation and electrode formation. The device shown in Fig. 1 was designed and fabricated by using these methods. The arrangement of the air holes shown in Fig. 1d is the result of optimizing the hole pattern in such a way to achieve an increased μ while keeping τ at a sufficient level (see Methods). Here, the design values of μ and τ of the optimized structure are 9 rad/ns and 36 ns, respectively. To avoid contamination of the nanocavity during fabrication, we used protective films during the activation annealing of the *p*- and *n*-regions, and used hydrofluoric acid (HF) vapor (instead of wet HF, which damages metal) to remove the SiO_2 underneath the PC after electrode formation (see Methods). The lifetimes and quality factors of nanocavities A, B, and C in our

fabricated sample were τ = 1.45 ns, 1.84 ns, and 0.71 ns, (Supplementary Fig. S3c) and Q = 1.75 million, 2.22 million and 0.86 million, respectively. The Supplementary Information explains how the lifetimes of nanocavities A and B were affected by the control cavity during the experiment. The coupling constant μ_{AC} (μ_{BC}), which characterizes the coupling between nanocavities A and C (B and C), was evaluated to be 9.4 (12.6) rad/ns (Supplementary Figs. S3a and S3b). By applying the average coupling constant $\mu = (\mu_{AC}+\mu_{BC})/2$ = 11 rad/ns to the optimal operation condition, the optimum value of $|d\lambda_C/dt|$ for efficient photon transfer is estimated to be 0.2 nm/ns. With the help of another sample, the actual value of $|d\lambda_C/dt|$ was estimated to be about 0.15 nm/ns when an electrical pulse with a voltage of 1.6 V and a duration of 8 ns was applied to the *p-i-n* junction (Supplementary Fig. S3d). This speed is in good agreement with the simulation of the carrier dynamics in the *p-i-n* structure (Supplementary Fig. S4b). We were able to control $|d\lambda_C/dt|$ in the range 0.15–0.43 nm/ns using voltages from 1.6 to 3.2 V (Supplementary Fig. S4b).

Demonstration of photon transfer from cavity A to B. We first adjusted the wavelengths of nanocavities A and B to reach the condition $\lambda_A - \lambda_B$ = 11.5 pm and $\lambda_C - \lambda_A$ = 150 pm. At this initial condition, the electromagnetic field distribution of the eigenstate at $\approx \omega_A$ consists almost entirely of the confined mode of nanocavity A (≈ 98%). Then we injected photons into this eigenstate (via the excitation waveguide) using a light pulse with a duration of 10 ns at a repetition rate of 5 MHz, and applied a synchronized voltage pulse with different delay times to the *p-i-n* diode while carrying out time-resolved measurements of the photons emitted from nanocavities A and B into free space (see Methods).

Figure 2a shows the measurement results for an electrical pulse with a voltage of 1.6 V and a duration of 8 ns. In this figure, the excitation of nanocavity A ends at the time $t \approx 1.9$ ns, and after this optical excitation the number of photons in nanocavity A decays with a constant lifetime (1.05 ns) until time t_1 (see the red curve). At time t_1, the effect of the voltage pulse becomes apparent: For times $t > t_1$, the number of photons in cavity A decays rapidly, and simultaneously the number of photons in cavity B (blue curve) increases correspondingly. This indicates the transfer of photons from cavity A to B. The number of photons in cavity B reaches its peak at time t_2, and for $t > t_2$, the number of photons in cavity B decays with a constant lifetime of 1.35 ns. Figure 2b shows the measurement results that were obtained when the timing of the voltage pulse was delayed by 1 ns compared to Fig. 2a. Except for the delay of the transfer by 1 ns, the behaviors of the photons in nanocavities A and B are almost the same as those in Fig. 2a. These experimental results clearly indicate that the photons stored in cavity A were transferred to cavity B by applying the voltage pulse, and we were able to control the transfer timing electrically.

In order to clarify the processes that govern the experimental results in Fig. 2a, we numerically calculated the time evolution of the coupled nanocavity system using the same conditions (see Supplementary Information). The calculated results are shown in Figs. 2c and 2d, where the former shows the value of λ_C relative to λ_A (the green curve) obtained from the simulation of the carrier dynamics in the *p-i-n* structure, and the latter shows the corresponding change of the optical energy in each nanocavity calculated by coupled mode theory. By comparing the optical energies in cavities A and B in Fig. 2d (the red and blue curves) with the experimental results in Fig. 2a, it can be seen that they are in good agreement. Furthermore, in Fig. 2c, the value of $|d\lambda_C/dt|$ near the intersections with the curves for λ_A and λ_B is about 0.16 nm/ns, which is also in agreement with the experimentally obtained value (0.15

nm/ns). This confirms that the experimental results in Fig. 2a show a spatial transfer of photons due to an adiabatic change of the eigenstate induced by increasing ω_C up to a frequency satisfying $\omega_B \ll \omega_C$.

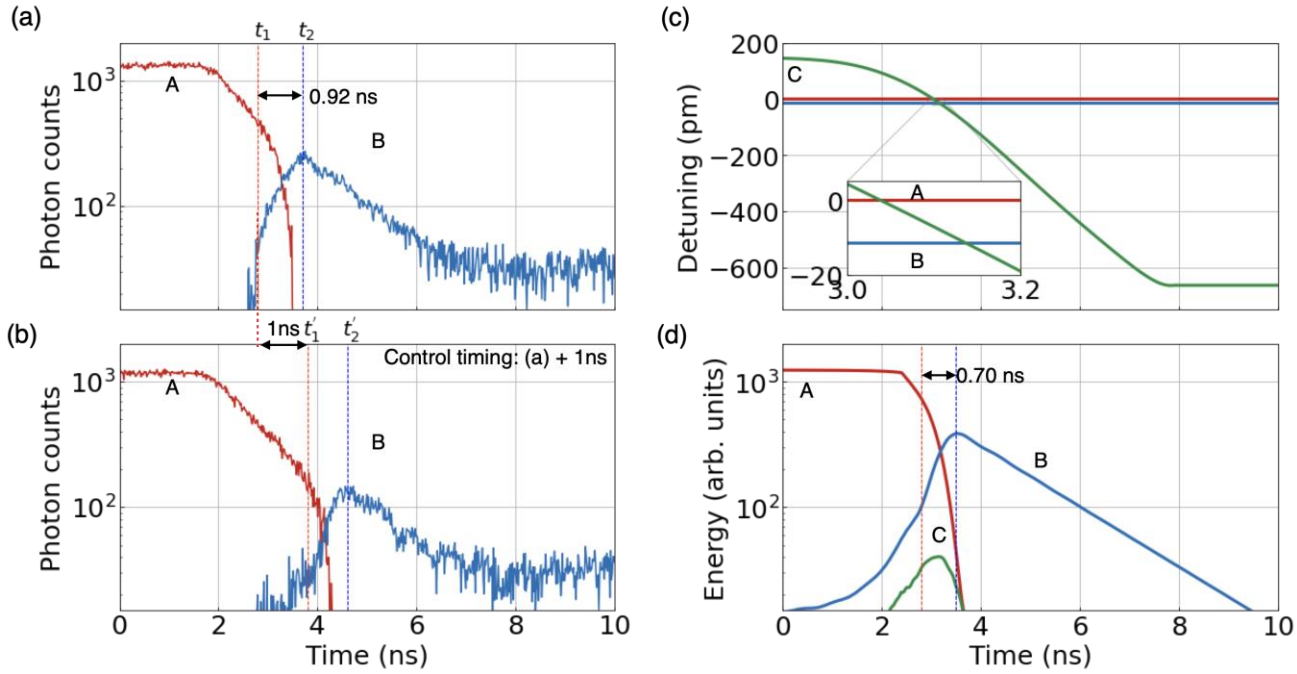

Fig. 2| Time-resolved signals from cavities A and B. (a) Experimental results of the photon transfer at a certain timing of the electrical control pulse, and (b) experimental results when the timing of the control pulse is delayed by 1 ns. (c) and (d) show calculation results corresponding to the experimental condition of (a). (c) The green curve shows the calculated change in λ_C relative to λ_A as a function of time, and (d) the shows the calculated optical energy contained in each nanocavity at a given time.

From the experimental data, we can also evaluate the transfer efficiency η, which is defined as the ratio of the number of photons in cavity B at the completion of the transfer to that in cavity A at the start of the transfer. As a practical criterion, we used the time when the time-resolved signal of nanocavity A begins to fall significantly as the start time (equivalent to the time when B begins to rise significantly, e.g. t_1 in Fig. 2a), and the time when the time-resolved signal of nanocavity B reaches its peak as the completion time (e.g. t_2 in Fig. 2a). This criterion almost coincides with the theoretical criterion discussed in the Supplementary Information. Using this criterion, we obtained η = 57% and 63% for Figs. 2a and 2b, respectively.

We also performed photon transfer experiments using different control-pulse voltages. Figure 3a plots the measured η versus the applied voltage amplitude. The values that are provided next to each data point in the figure, are the corresponding $|d\lambda_C/dt|$ values estimated from the simulation of the *p-i-n* structure. Note that $|d\lambda_C/dt|$ increases with the applied voltage (Supplementary Fig. S 4b), because it controls the injection current. As discussed above, the ideal photon transfer efficiency determined by the adiabatic condition is higher for smaller $|d\lambda_C/dt|$ values. On the other hand, in a non-ideal system, the loss of photons due to free-carrier absorption in cavity C and the intrinsic loss in cavities A and B during $\omega_A \leq \omega_C \leq \omega_B$ is lower for larger $|d\lambda_C/dt|$ values. This results in a maximum of η at intermediate voltages. The photon transfer efficiency obtained using a voltage of 1.8 V was the highest (η = 76%), and the

corresponding time-resolved data is shown in Fig. 3b. The estimated $|d\lambda_C/dt|$ at this applied voltage is 0.2 nm/ns, which is consistent with the theoretical optimum of 0.2 nm/ns.

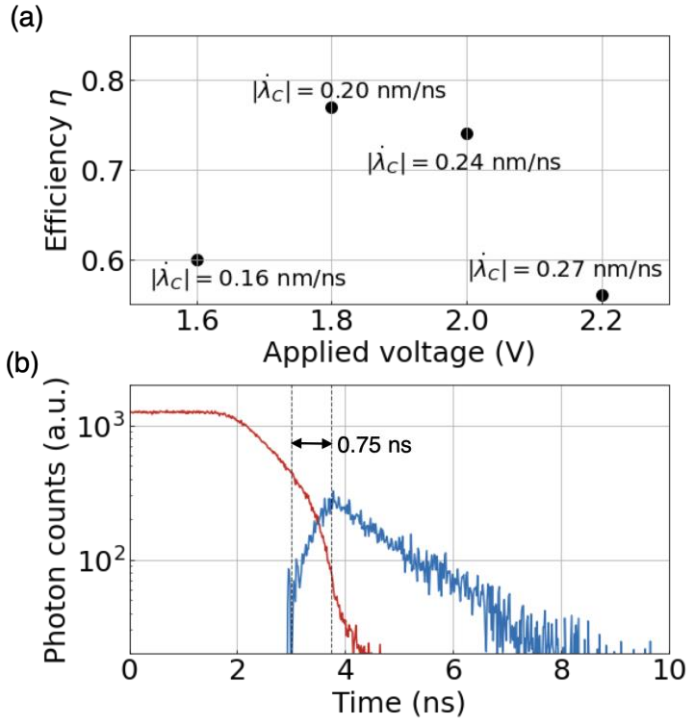

Fig. 3| Voltage dependence of the photon transfer efficiency. (a) Transfer efficiency as a function of the control-pulse voltage. The number next to each data point is the corresponding $|d\lambda_C/dt|$. (b) Results of the photon transfer experiment with a pulse amplitude of 1.8 V, where the maximum transfer efficiency of 76% was obtained.

Discussion

Here we consider several factors that can be used to further improve the electrically controlled photon transfer between PC nanocavities. Firstly, we characterized the decay time constants of the photons in the transfer experiment and the time required for the photon transfer as shown in the Supplementary Information. The results indicate that the carrier densities in cavity C during the transfer and the detuning between λ_B and λ_C after the transfer need to be considered, and that the measured transfer times are consistent with the predictions within the measurement resolution.

Secondly, if we assume a control cavity with a lifetime of $\tau_C = 10$ ns at zero bias, the *i*-layer width can theoretically be reduced to 3 μm, and $|d\lambda_C/dt|$ can theoretically be increased to 0.7 nm/ns using a pulse voltage of 3 V (see Supplementary Information). Because we have already fabricated nanocavities with lifetimes of 9.2 ns,[7] fabrication of nanocavities with significantly longer lifetimes should be possible by reducing the absorption loss due to contamination and the scattering loss due to structural fluctuations by 75%. Therefore, we assume that we can design and fabricate a coupled nanocavity system where $\tau_A = \tau_B = 36$ ns (at zero bias) and $\tau_C = 10$ ns while μ is large enough to satisfy $|d\omega_C/dt| \simeq 0.2 \times 2\pi\mu^2$ for the considered high value of $|d\lambda_C/dt| = 0.7$ nm/ns. The optimum μ required for this increased $|d\lambda_C/dt|$ is only 1.9 times larger than the present value, and the assumed long lifetime of 36 ns should be compatible with this larger μ. The required reduction in the contaminations is considered possible by using

protective films in other fabrication steps besides activation annealing as well. The required reduction of the fluctuations of air hole positions and radii will require further improvements of the electron-beam writing and dry etching processes. If this can be achieved, the transfer time is 0.39 ns and the transfer efficiency is 97% as shown by the numerical results in Fig. 4. Although the optical energy in cavity C during the photon transfer in this system is larger than that in the case of Fig. 2d due to the fact that μ is 1.9 times larger, the total free-carrier loss is almost the same owing to the shorter transfer time. Furthermore, the loss in cavities A and B during the transfer is significantly lower owing to the longer lifetimes and the shorter transfer time, resulting in the higher transfer efficiency of 97%.

From the viewpoint of the application of such a system as an optical buffer, operation at GHz frequencies is required. Note that the operating frequency depends not only on the carrier injection rate but also on the carrier extraction rate and the carrier lifetime. Therefore, it is necessary to optimize the electrical characteristics of the *p-i-n* junction to enable an improved operating frequency. Switching to electro-optical materials, such as thin-film lithium niobate[17] and silicon carbide[18,19], may be another solution. Such materials are also advantageous in avoiding free-carrier absorption, which accompanies the refractive index control by the carrier plasma effect. Moreover, the narrow bandwidth of storage nanocavities with high Q factors is another factor that needs to be considered, because the efficiency of coupling of an optical pulse into a nanocavity is lower when the duration of the pulse is shorter than the cavity lifetime. This problem can be solved by developing an electrical implementation of dynamical control of the Q factor of a nanocavity[20].

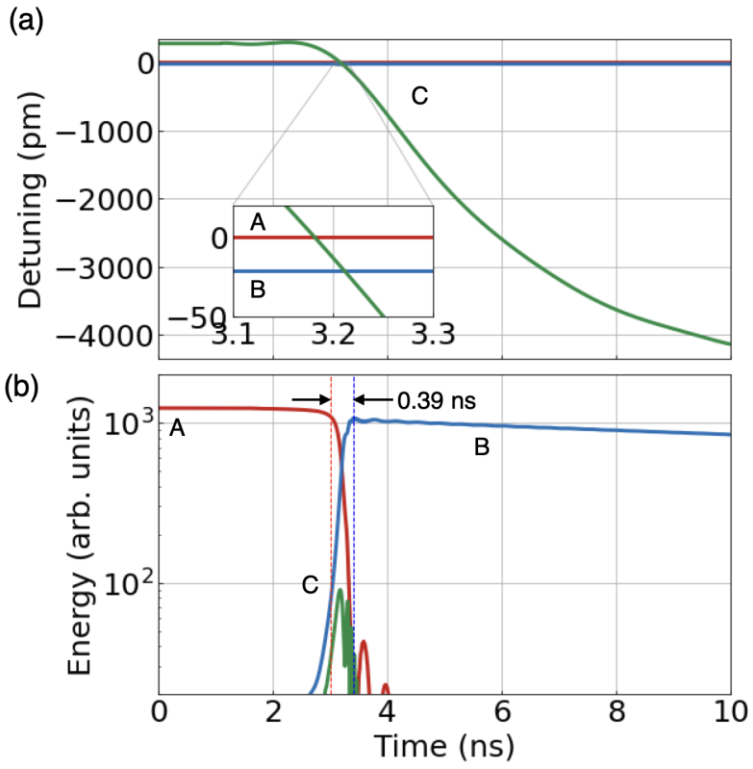

Fig. 4| Expected photon transfer characteristics of an improved structure. (a) Theoretical time dependence of the relative position of λ_C (green curve), and (b) the corresponding energy distribution in the three cavities as a function of time. Here, we assumed a reduction of the *i*-layer width to 3 μm and

3-V control pulse. The coupling constant was assumed to be large enough to fulfill the adiabatic condition for the increased speed of the resonance-wavelength shift of nanocavity C. The cavity lifetimes were assumed to be 36 ns, 36 ns, and 10 ns for nanocavities A, B, and C, respectively.

In conclusion, we have demonstrated an ultra-high *Q*-factor nanocavity system on a single Si chip that allows us to transfer photons stored in one nanocavity to another nanocavity at an arbitrary timing by using an electrical control pulse. This result is a significant advance compared to the previous proof-of-concept experiment using optical pulses for control, because the present integrated system does not require a huge external optical system for control and enables complex timing control. Despite the realized large nanocavity coupling constants (required for efficient and fast photon transfer) and the integration of the *p-i-n* diode (required for the electrical control), the photon lifetime after the photon transfer was 1.3 ns, which is 6.5 times longer than the value achieved in the previous study (200 ps). This improvement is a result of the developed design and fabrication methods. The integration of an electrical refractive-index-control mechanism and the improvement of the photon lifetimes are important results, because they enable scaling up to optical buffering memories that use many coupled nanocavities. In addition, the electrical control via the *p-i-n* diode allows both fast injection of carriers and also their extraction, which may lead to new control schemes of coupled-cavity systems that can be advantageous for various applications[21–23]. We hope that future advances in the operating speed, the system scale, and the control scheme, will lead to optical buffering without need of conversion between electrical and optical signals, which could significantly reduce energy consumption and latency at the nodes of optical fiber communication networks.

Methods

Optimization of the PC structure

The arrangement of the air holes located between the nanocavity and the waveguide is not exactly that of the PC lattice; the arrows in Fig. 1d show the displacements of the actual hole positions with respect to the original PC lattice. This new arrangement was obtained by optimizing the hole pattern in such a way to achieve a sufficient coupling constant while suppressing radiation losses due to disturbance of the mode distribution. The design method used for this work is an extension of our previously developed method[10], which uses deep neural networks to learn the relationship between the air hole positions and the selected target parameter of the system[24]. More concretely, we first adjusted the position of the coupling waveguide with respect to the nanocavity roughly by using first principle simulations of the electro-magnetic field (finite-difference time-domain method: FDTD method). Next, we set τ and μ as the target parameters, and let a deep neural network learn the relationship between the air hole displacements and τ and μ by using many example patterns generated by randomly displacing the positions of the air holes in the area shown in the blue dashed rectangle of Fig. 1d. Then, we repeatedly searched for new structures that have lager τ and μ values by using the trained deep neural network, and updated the example patterns used for learning by adding the obtained new structures until the new results obtained by the re-trained neural network saturate. The design τ and μ values of the optimized structure are 36 ns and 9 rad/ns, respectively, while those of the structure before optimization are 8.3 ns and 3.8 rad/ns, respectively. Details will be published separately.

Device fabrication

The samples were fabricated using SOI substrates with a top Si layer thickness of 220 nm and a buried oxide (BOX) layer thickness of 3 μm. The *p*- and *n*-regions near nanocavity C were formed by electron beam (EB) patterning and ion implantation, respectively, followed by formation of a protective film and activation annealing in a quartz furnace. Then, the PC structure shown in Fig. 1 was patterned by EB lithography and transferred to the top Si layer by inductively coupled plasma reactive ion etching (ICP-RIE). The diameter of the air holes constituting the PC was set to 220 nm. After patterning of the electrodes, Al electrodes with a thickness of 400 nm were formed by EB deposition, and lift-off was carried out. Then, the BOX layer at the bottom of the nanocavity was removed using HF gas. Finally, the chip containing the coupled nanocavity system was mounted on a ceramic package and wire bonded.

Time-resolved measurements

In the photon transfer experiment, an optical pulse was introduced into the excitation waveguide of the sample to excite nanocavity A, and an electrical pulse was applied to the *p*-*i*-*n* structure of nanocavity C. The optical pulse was generated by modulating the output of a wavelength tunable laser (Santec TSL710) using a lithium niobate modulator (EOSPACE) to obtain a rectangular pulse with a repetition rate of 5 MHz (repetition period 200 ns) and a width of 10 ns. The optical pulse was synchronized with the electrical control pulse with a width of 8 ns and a voltage in the range of 1.6–2.2 V generated by a pulse generator (Agilent 81110A). The photons emitted from nanocavities A and B into free space were observed using a photomultiplier tube (Hamamatsu photonics H12397A-75) and a time-correlated single-photon counting (TCSPC) module (PicoHarp PH-300). Since the intrinsic photon emission probability of each nanocavity is independent of time, the measured emission intensities are proportional to the number of photons stored in a nanocavity. The degree of the difference between the detection efficiencies of the photons from nanocavities A and B was evaluated using the eigenstate where the spatial modes of nanocavities A and B overlapped with equal weight, which occurs when λ_B is tuned to the value of λ_A using the microheater. The ratio of the detection efficiency of nanocavity A to that of B was 63%. We corrected the data for this difference. The time-resolved measurements were carried out separately: after the measurement of the emission from one storage cavity, the objective lens was moved to the other storage cavity within a few minutes, and then the photon emission of this cavity was measured. The results shown are those after removing the background and compensating for the different excitation power and the detection efficiency.

References

1. Noda S., Recent progresses and future prospects of two- and three-dimensional photonic crystals, *J. Light. Technol.* **24**, 4554 (2006).
2. Baba T., Slow light in photonic crystals, *Nat. Photon.* **2**, 465 (2008).
3. Reed G. T., Mashanovich G., Gardes F. Y., Thomson D. J., Silicon optical modulators, *Nat. Photonics* **4**, 518 (2010).

4. Arakawa Y., Nakamura T., Urino Y., Fujita T., Silicon photonics for next generation system integration platform, *IEEE Commun. Mag.* **51**, 72 (2013).

5. Asano T., Noda S., Photonic Crystal Devices in Silicon Photonics, *Proc. IEEE* **106**, 1 (2018).

6. Jones R. *et al.*, Heterogeneously Integrated InP/Silicon Photonics: Fabricating fully functional transceivers, *IEEE Nanotechnol. Mag.* **13**, 17 (2019).

7. Asano T., Ochi Y., Takahashi Y., Kishimoto K., and Noda S., Photonic crystal nanocavity with a Q factor exceeding eleven million, *Opt. Express* **25**, 1769 (2017).

8. Konoike R., et al., On - demand transfer of trapped photons on a chip, *Sci. Adv.* **2**, e1501690 (2016).

9. Song B.-S., Noda S., Asano T., Akahane Y., Ultra-high-Q photonic double-heterostructure nanocavity, *Nat. Mater.* **4**, pp. 207–210 (2005).

10. Asano T. and Noda S., Optimization of photonic crystal nanocavities based on deep learning, *Opt. Express* **26**, 32704 (2018).

11. Tanabe T., Nishiguchi K., Kuramochi E., and Notomi M., Low power and fast electro-optic silicon modulator with lateral p-i-n embedded photonic crystal nanocavity, *Opt. Express* **17**, 22505 (2009).

12. Cocorullo G., Della Corte F. G., and Rendina I., Temperature dependence of the thermo-optic coefficient in crystalline silicon between room temperature and 550 K at the wavelength of 1523 nm, *Appl. Phys. Lett.* **74**, 3338 (1999).

13. Sato Y., et al., Strong coupling between distant photonic nanocavities and its dynamic control, *Nat. Photon.* **6**, 56 (2012).

14. Konoike R., Sato Y., Tanaka Y., Asano T., and Noda S., Adiabatic transfer scheme of light between strongly coupled photonic crystal nanocavities, *Phys. Rev. B* **87**, 165138 (2013).

15. Zener C., Non-adiabatic crossing of energy levels, *Proc. of the Royal Society of London*. Series A, Containing Papers of a Mathematical and Physical Character, **137**, 696 (1932).

16. Borselli M., Johnson T. J., Painter O., Measuring the role of surface chemistry in silicon microphotonics, *Appl. Phys. Lett.* **88**, 2005–2007 (2006).

17. Li M., Liang H., Luo R., He Y., Ling J., Lin Q., Photon-level tuning of photonic nanocavities, *Optica* **6**, 860 (2019).

18. Song B.-S., Asano T., Jeon S., Kim H., Chen C., Kang D. D., Noda S., Ultrahigh-Q photonic crystal nanocavities based on 4H silicon carbide, *Optica* **6**, 991 (2019).

19. Lukin D. M., Dory C., Guidry M. A., Yang K. Y., Mishra S. D., Trivedi R., Radulaski M., Sun S., Vercruysse D., Ahn G. H., Vučković J., 4H-silicon-carbide-on-insulator for integrated quantum and nonlinear photonics, *Nat. Photonics* **1**, 10 (2019).

20. Tanaka Y., Upham J., Nagashima T., Sugiya T., Asano T., Noda S., Dynamic control of the Q factor in a photonic crystal nanocavity, *Nat. Mater.* **6**, 862 (2007).

21. Konoike R., Asano T., Noda S., On-chip dynamic time reversal of light in a coupled-cavity system, *APL Photonics* 4, 030806 (2019).

22. Fang K., Yu Z., Fan S., Realizing effective magnetic field for photons by controlling the phase of dynamic modulation, *Nat. Photonics* **6**, 782 (2012).

23. Estep, N., Sounas, D., Soric, J., Alu A., Magnetic-free non-reciprocity and isolation based on parametrically modulated coupled-resonator loops. *Nature Phys* **10,** 923 (2014).

24. Asano T. and Noda S., Iterative optimization of photonic crystal nanocavity designs by using deep neural networks, *Nanophotonics* **8**, 2243 (2019).

Acknowledgements

We thank B. S. Song for fruitful discussions. This work was partially supported by KAKENHI Grant Numbers 18J23217 and 19H02629, and received funding from the New Energy and Industrial Technology Development Organization (NEDO) under Grant Number JPNP13004.

Author contributions

M.N. developed the fabrication process and performed the experiment. T.A. set up the measurement system and performed the simulations of the p-i-n structure. T.A. and S.N. designed the study. All authors analyzed the results and contributed to the writing of the manuscript.

Data Availability

The authors declare that the all the data supporting the findings of this study are available within this article and its Supplementary Information files, and are also available from the corresponding author upon reasonable request.

Code availability

All associated codes for simulations are available from the corresponding author upon reasonable request.

Additional information

The authors declare no competing financial interests. Supplementary information accompanies this paper at www.nature.com/naturephotonics. Reprints and permission information is available online at http://www.nature.com/reprints. Correspondence and requests for materials should be addressed to M.N. and T.A.

Supplementary Information

Expanded view of the designed structure

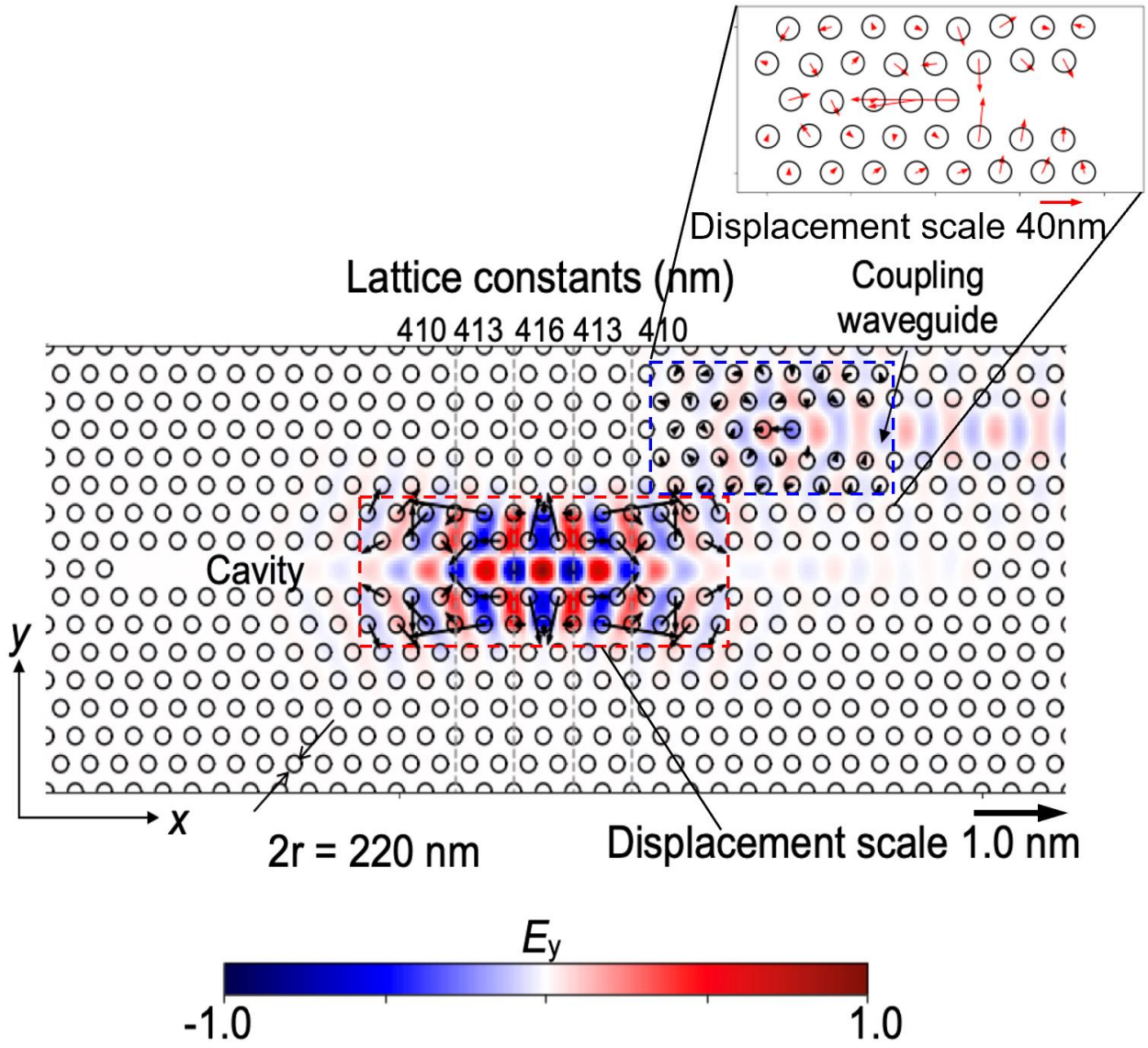

Fig. S1| Expanded view of the designed hole pattern for nanocavity A and the left coupling waveguide shown in Fig. 1(d). The result of the fine tuning of the air hole positions is shown by the displacement arrows. The length scale of the arrows of the cavity region is indicated below the figure, and that of the waveguide region is indicated above. The radii of the air holes are r = 110 nm. The distribution of the y component of the electric field of the resonant mode is plotted with blue and red colors.

Operating principle

In this coupled nanocavity system, photons can be transferred adiabatically from nanocavity A to B by changing the resonance frequency of nanocavity C, similar to the mechanism explained in the previous study[8]. The coupled cavity system has three eigenstates composed of superpositions of nanocavities A, B, and C, where we define angular resonance frequencies of the nanocavities (without coupling) as ω_A, ω_B, and ω_C, respectively. When ω_C is changed, the three eigenfrequencies of the system change continuously as shown in Fig. S2. Near the point where ω_C crosses

ω_A, an anti-crossing of the eigenstates occurs due to the coupling between nanocavities A and C (with strength μ), and a similar anti-crossing occurs when ω_C crosses ω_B. When we focus on the trajectory of the eigenstate in the middle of the frequency range in Fig. S2 (highlighted in yellow), we can see that its spatial mode is almost that of the confined mode of nanocavity A when $\omega_C \ll \omega_A$ (see the left inset). On the other hand, it becomes a superposition of those of nanocavities A, B, and C when $\omega_A \leq \omega_C \leq \omega_B$ (see the center inset), and is almost like that of nanocavity B when $\omega_B \ll \omega_C$ (see the right inset). When we set $\omega_C \ll \omega_A$, we can inject photons into nanocavity A by exciting the system at ω_A, because its confined mode contributes the most to the eigenstate at $\approx \omega_A$ under this condition. Furthermore, we can transfer the photons from nanocavity A to nanocavity B by simply increasing ω_C up to a frequency satisfying $\omega_B \ll \omega_C$[14]. According to the adiabatic theorem, if the speed of the change in ω_C ($d\omega_C/dt$) is infinitesimal, all photons can be transferred from cavity A to B because the photons stay on the eigenstate that continuously evolves with respect to the change of the system (adiabatic transition). However, $d\omega_C/dt$ needs to be finite in reality and transitions to other eigenstates occur, which reduces the number of photons transferred to nanocavity B. This deviation from the adiabatic approximation has been analyzed in detail by Landau and Zener[15]. Based on their analysis, the fraction p of photons that transit to another eigenstate at a given anti-crossing condition (determined by ω_C as shown in Fig. S1) is determined by the relation between $d\omega_C/dt$ and the coupling constant μ,

$$p = \exp\left(-\frac{2\pi\mu^2}{|\,d\omega_c/dt|}\right). \tag{S1}$$

Therefore, in order to increase the photon transfer efficiency by reducing p, it is necessary to set $|d\omega_C/dt|$ to a value that is significantly smaller than $2\pi\mu^2$. However, when we use free-carrier injection to control ω_C, a loss will occur in the region $\omega_A \leq \omega_C \leq \omega_B$, because here the photons partially exist in nanocavity C and free-carrier absorption takes place. To avoid this loss, we need to increase $|d\omega_C/dt|$ and pass through this region quickly. Several factors, including this trade-off relation, determine the optimum operating point. According to a detailed theoretical study[14], the highest transfer efficiency can be achieved by adjusting the difference between ω_A and ω_B to about 0.8μ and then adjusting $|d\omega_C/dt| \simeq 0.2 \times 2\pi\mu^2$, if the photon lifetimes in the cavities (without free carriers) are sufficiently long. Here, the theoretical transfer time is defined as the time required from the start of the first anti-crossing until the end of the second anti-crossing. The theoretical transfer time is estimated to be about $6/\mu$ under the optimum condition.

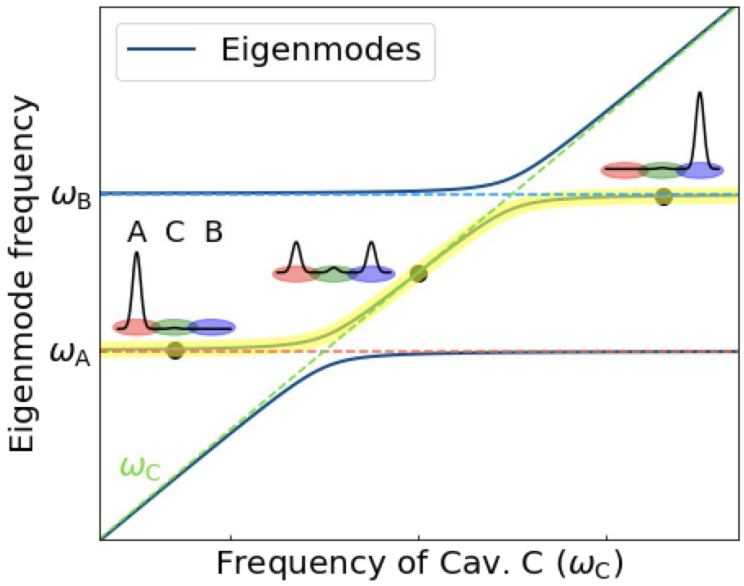

Fig. S2| Conceptual diagram showing the eigenstates of the system when the resonance frequency of nanocavity C is changed.

Basic evaluation of the fabricated samples

Figure S3a shows the resonance wavelengths of nanocavities A, B, and C (λ_A, λ_B, and λ_C, respectively) as a function of the power applied to the microheater in the vicinity of nanocavity A. Figure S3b shows the changes of λ_A, λ_B, and λ_C that occurred when the other microheater was used. It can be confirmed that λ_A and λ_B can be controlled almost independently over a range of about 1 nm by using the microheaters. By theoretically analyzing the data near the anti-crossing of λ_A and λ_C in Fig. S3a (see inset), we determined a value of 9.4 rad/ns for the coupling constant μ_{AC}, which describes the strength of the coupling between nanocavities A and C. Similarly, from Fig. S3b, μ_{BC} = 12.6 rad/ns was obtained. By applying the average value of the two coupling constants $\mu = (\mu_{AC}+\mu_{BC})/2$ = 11 rad/ns to the optimal operation condition (i.e. $|d\omega_C/dt| \simeq 0.2 \times 2\pi\mu^2$ as described in the previous section) and using the relation $|d\lambda/dt| = \lambda/\omega \times |d\omega/dt|$, we estimated that the speed of the resonance-wavelength shift of nanocavity C required for an efficient photon transfer is $|d\lambda_C/dt| \approx 0.2$ nm/ns.

To measure the photon lifetimes of the three nanocavities, the microheaters were switched off, because under this condition the nanocavities A, B, and C are almost independent. The time-resolved measurement results of the cavity photons in Fig. S3c show that the photon lifetimes of nanocavities A, B and C are 1.45 ns, 1.84 ns, and 0.71 ns, respectively (the decay in the range below 10^3 counts is slower probably due to the background noise or an imperfect extinction ratio of the input pulse, and thus we evaluated the lifetimes at the initial stage of the decay). The corresponding quality factors are 1.75 million, 2.22 million and 0.86 million, respectively. On the other hand, the theoretically predicted photon lifetime is 36 ns. The relatively short photon lifetimes are attributed to fabrication imperfections (e.g. random variations of the hole positions) and residual contamination of the nanocavity[7,16,S1].

Furthermore, we also tried to measure the value of $|d\lambda_C/dt|$ while applying an electrical pulse to the *p-i-n* diode that contains nanocavity C in the *i*-layer. However, we were not able to measure the resonance-wavelength dynamics, because the observed photon emission from nanocavity C was too weak. Therefore, another sample with the same structure was used for the estimation of $|d\lambda_C/dt|$. Figure S3d shows a representative result of the resonance-wavelength dynamics for the case of a control pulse with a voltage of 1.6 V and a width of 8 ns (the details of this measurement are explained in the next section). The estimated timing of the signal from the pulse generator is shown on the top. It can be seen that the peak wavelength begins to shift to shorter wavelengths after the rise of the voltage. The peak-shift saturates at around 8 ns where it reaches a value of -0.55 nm, and after the voltage pulse, the peak returns to the original position. The speed of the resonance-wavelength shift shown by the dashed line in Fig. S3d, is about 0.15 nm/ns. This speed is in good agreement with the simulation result of the carrier dynamics in the *p-i-n* structure (Supplementary Fig. S4b). Since the sample used for the photon transfer experiment shows almost the same I–V characteristics as the sample used to prepare Fig. S3d (Supplementary Fig. S4a), we assumed that the wavelength-shift characteristics of the two samples are similar, and used the abovementioned simulation results (including those for other applied voltages) for the analysis of the photon transfer experiment.

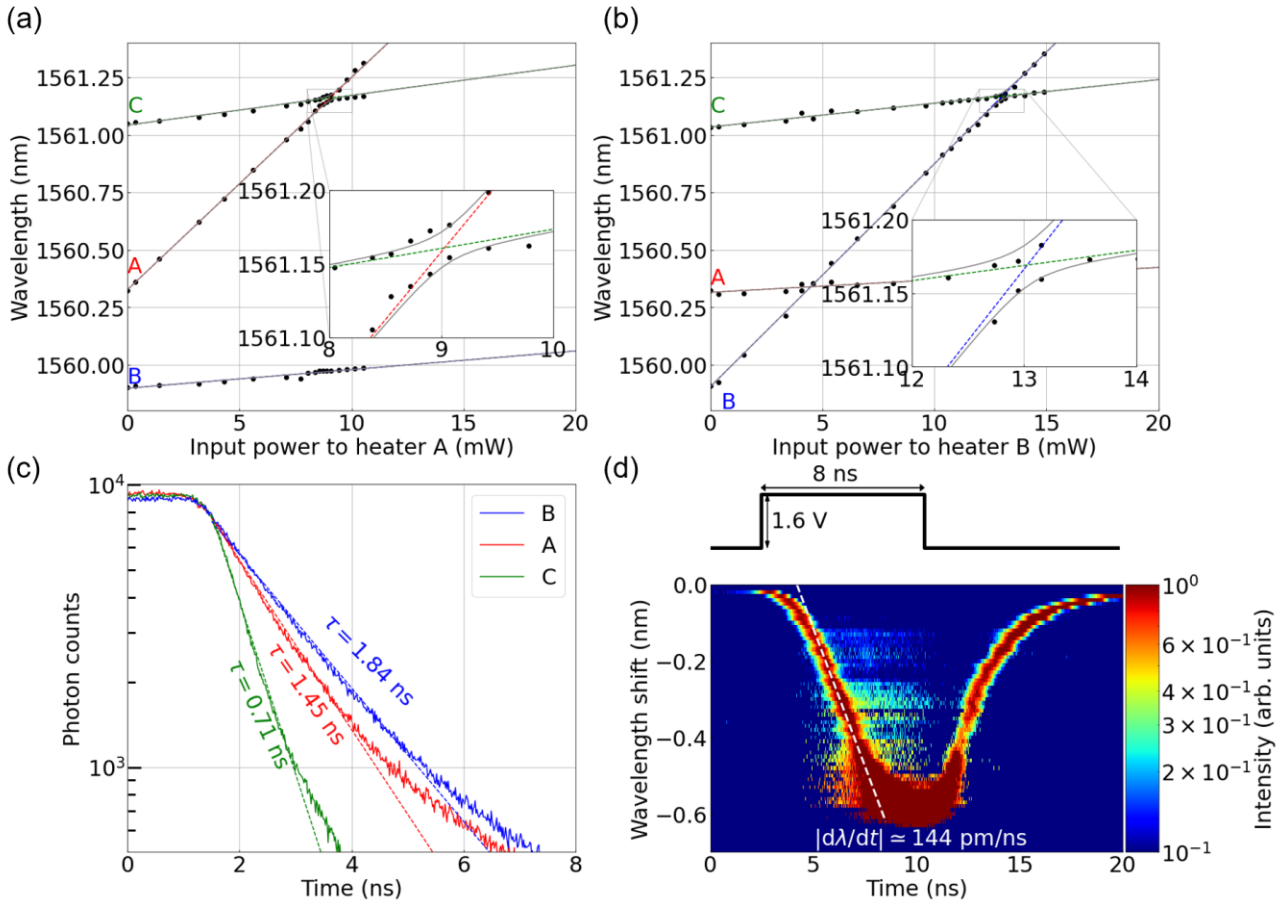

Fig. S3| Basic evaluation of the fabricated device with both photonic and electronic components. (a), (b) The peak wavelengths of the resonance spectra observed at the positions of nanocavities A, B, and C as a function of the electrical power applied to the heater near nanocavity A and B, respectively. The cavity–cavity coupling constants can be evaluated from the anti-crossing behavior shown in the insets.

(c) Decay curves of the photons emitted from nanocavities A, B, and C. (d) Time-resolved measurement of the resonance wavelength of the control nanocavity in another sample for a control pulse with a voltage of 1.6 V.

Estimation of the resonance-wavelength dynamics of a cavity in a *p-i-n* structure

When a voltage pulse is applied to a *p-i-n* diode, injection and extraction of carriers occurs and the refractive index changes due to the carrier-plasma effect. Therefore, the resonance wavelength of a cavity located in the *i*-region can be changed dynamically. The following experiment was used to estimate the speed of the resonance-wavelength shift caused by a voltage pulse. The measurement system was almost the same as that described in the Methods, but the incident light was continuous-wave (CW) light. When the time-resolved photon emission from a nanocavity is measured while the nanocavity is excited by CW light, a signal will appear only during the time period when the resonance wavelength of the nanocavity coincides with the wavelength of the excitation light. By performing this measurement for various wavelengths and reconstructing the results, the resonance-wavelength dynamics as shown in Fig. S3(d) can be obtained.

For this measurement, we need to be able to observe the radiation from the nanocavity in the *i*-layer even in a state where carriers have been injected and the optical absorption has increased. However, although the sample used in the optical transfer measurement (Figs. 1 to 3) showed good I–V characteristics (black curve in Fig. S4a), the detection efficiency of photons from nanocavity C was low, and thus it was not possible to measure the time-resolved photon emission from nanocavity C in the transient state induced by the voltage pulse. This low detection efficiency may be a result of the radiation pattern, which can be distorted by the random variations of the hole geometry. Therefore, we performed the abovementioned measurements on another sample with the same structure as that of the sample shown in Fig. 1. The I–V curve of the sample for the measurement of the wavelength dynamics are shown in Fig. S4a as the red solid curve; both samples exhibit similar I–V characteristics. The temporal evolution of the resonance wavelength due to a control pulse with a voltage of 1.6 V is shown in Fig. S3d. Based on this data, we consider that the typical speed of the resonance-wavelength shift is ≈ 0.15 nm/ns at 1.6 V. The same measurements were carried out for voltages up to 3.2 V. The red dots in Fig. S4b show the obtained values of the speed of the resonance-wavelength shift for various applied voltages; a larger applied voltage results in a faster change, and the speed at 3.2 V is 0.43 nm/ns. Unfortunately, this sample was subsequently damaged by electro static discharge (ESD). Therefore, we were not able to measure the photon transfer in this sample.

In order to verify the experimental results of the resonance-wavelength dynamics, we analyzed the carrier dynamics in a *p-i-n* diode. For simplicity, we approximated the *p-i-n* diode of the sample as a one-dimensional structure. First, we solved the equation system consisting of (a) the diffusion equation including recombination, (b) the Poisson equation, and (c) the equation for the displacement current to obtain the time evolution of the carrier distribution. We used the standard method described in the literature[S2,S3]. Then, the refractive index change Δn was calculated from the carrier density[S4], and finally the resonance-wavelength change $\Delta\lambda$ was calculated using

$$\Delta\lambda = \frac{\Gamma\Delta n}{n}\lambda_0, \tag{S2}$$

where n = 3.46 is the refractive index of Si, λ_0 is the initial resonance wavelength (assumed to be 1560 nm), and Γ is the optical confinement factor (= 0.8). The analytical results are shown by the solid blue curve in Fig. S4b, and are consistent with the experimental results.

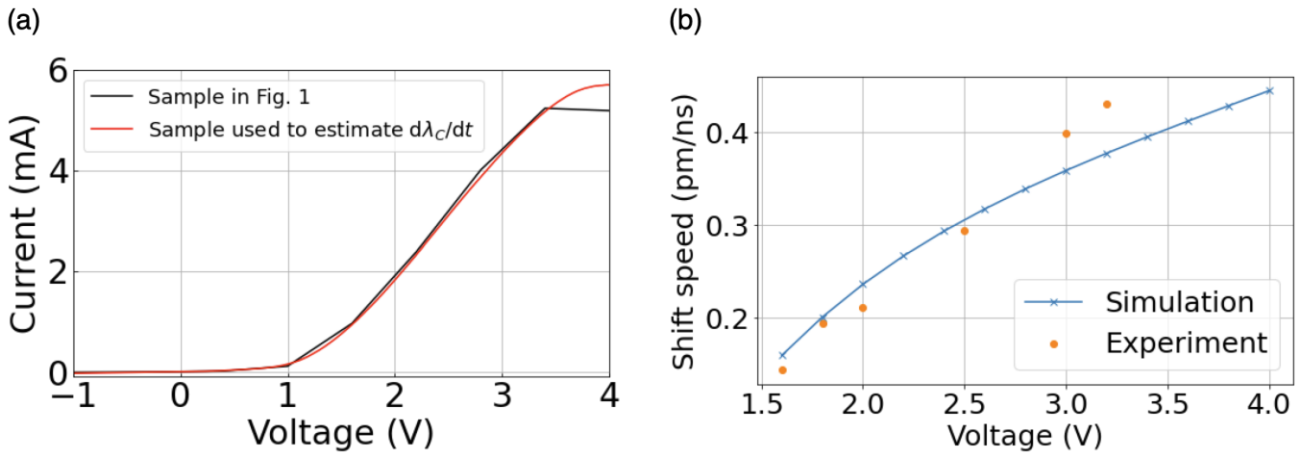

Fig. S4| (a) I–V characteristic of the *p-i-n* structure of the sample shown in Fig. 1 (black curve) and that of the sample used to measure the speed of the resonance-wavelength shift (red curve). (b) Experimental and numerical results of the speed of the resonance-wavelength shift as a function of the applied voltage.

Numerical simulation of the photon transfer

By using the simulation results of the resonance-wavelength dynamics of nanocavity C obtained in the above section, we calculated the time evolution of the coupled cavity system by numerically solving the corresponding coupled mode equations. Here, the actually measured lifetimes of nanocavities A and B, and the absorption loss due to the carrier injection into nanocavity C were taken into account.

Comparison with previous studies

In order to compare our results with those of the previous proof-of-concept demonstration for (optically controlled) photon transfer between nanocavities[8], we performed simulations in which the photon lifetimes of nanocavities A and B (without the influence of nanocavity C) are set to infinity. In this simulation, we only considered the absorption loss in nanocavity C (the radiation losses of the nanocavities were zero). For the other parameters we used the same values as those used in the calculations for Fig. 3. The results are shown in Fig. S5. When the transfer efficiency is defined as the ratio of the peak value of the energy in nanocavity B after the transfer to the energy in nanocavity A before transfer (see the broken lines), which is the same criterion as in our previous study, a value of 91.3% is obtained. This value is almost the same as the maximum efficiency of 90% reported previously[8].

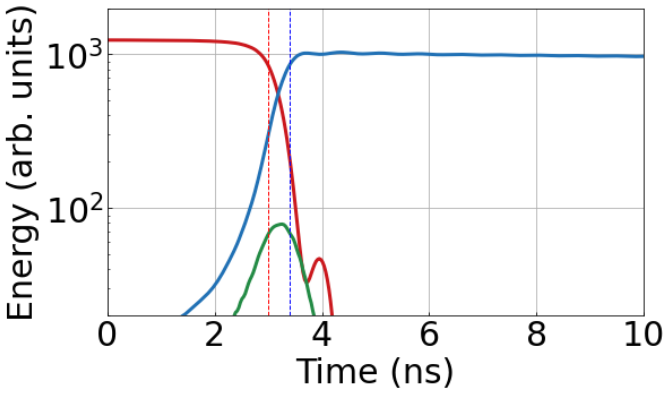

Fig. S5| Theoretical photon-transfer characteristics when the photon lifetimes of the nanocavities A and B are assumed to be infinite.

Decay time constants during the transfer experiment

The decay time constants of the photons evaluated from the slopes of the curves in Fig. 2a were 1.05 ns and 1.35 ns for nanocavity A and B, respectively. In contrast, the corresponding τ values obtained when λ_A, λ_B, and λ_C were largely detuned, were 1.45 ns and 1.84 ns, indicating that the lifetimes were slightly reduced during the transfer experiment. This reduction can be explained by the difference in the contribution of nanocavity C to the eigenstate; in the initial state of the transfer experiment, the difference between λ_C and λ_A was about 150 pm, and thus about 2% of the light with wavelength λ_A was located in nanocavity C. Since the τ of nanocavity C, τ_C, was relatively short (0.75 ns), the τ of the initial state was reduced due to the superposition of nanocavity C. After the transfer, λ_C remained at about 400 pm below λ_B, where the superposition of nanocavity C still had a detrimental effect because a large number of carriers had been injected and the carrier density was still high. The τ in the initial state can be improved if both the lifetimes of nanocavities A and C (without carriers) are increased. As for the lifetime after the transfer, a further increase of the detuning between λ_B and λ_C after the transfer will prevent the influence of the carriers in cavity C. To reduce the loss of photons in the range $\lambda_C > \lambda_B$, the reduction of the carrier density in nanocavity C at these times is important. In a system with a longer τ_C in the absence of electrically injected carriers, we can set λ_C to values closer to λ_A and λ_B in the initial state, resulting in smaller carrier densities at these times.

Comparison between experimental and theoretical photon transfer times

The time required for the photon transfer was about 0.92 ns when the pulse voltage was 1.6 V as shown in Fig. 2a. When the pulse voltage was 1.8 V (Fig. 3b), which resulted in the maximum transfer efficiency, the transfer time was about 0.75 ns. Theoretically, the photon transfer time is about $6/\mu$ under the optimum condition (see the discussion on the operating principle in the Supplementary Information), resulting in 0.55 ns using the average coupling constant $\mu = 11$ rad/ns. The experimentally determined transfer time for 1.8 V was longer than 0.55 ns, but this is reasonable considering the time resolution of the measurement system (~ 0.4 ns). To further reduce the transfer time while keeping the transfer efficiency at the same level, it is necessary to improve both the carrier injection rate into nanocavity C and μ while maintaining $|d\omega_C/dt| \simeq 0.2 \times 2\pi\mu^2$. While reducing the *i*-layer width can improve the former,

this can unfortunately also reduce τ_C due to the increase in the carrier density at zero bias. According to theoretical calculations, if we accept a reduction of τ_C down to 10 ns, the *i*-layer width can be reduced to 3 μm, and $|d\lambda_C/dt|$ can be increased to 0.7 nm/ns when the pulse voltage is 3 V.

References

[S1] M. Nakadai, K. Tanaka, T. Asano, Y. Takahashi, S. Noda, "Statistical evaluation of Q factors of fabricated photonic crystal nanocavities designed by using a deep neural network," *Appl. Phys. Express* **13**, 012002 -1-5, (2020).

[S2] D. L. Sharfetter, H. K. Gummel, "Large-Signal Analysis of a Silicon Read Diode Oscillator," *IEEE Trans. Electtron Devices* **ED-16**, pp. 64–77 (1969).

[S3] G. D. Hachtel, R. C. Joy, J. W. Cooley, "A New Efficient One-Dimensional Analysis Program for Junction Device Modeling," *Proc. IEEE* **60**, pp. 86–98 (1972).

[S4] M. Nedeljkovic, R. Soref, G. Z. Mashanovich, "Free-carrier electrorefraction and electroabsorption modulation predictions for silicon over the 1-14-μm infrared wavelength range," *IEEE Photonics J.* **3**, pp. 1171–1180 (2011).